RSC Advances

ROYAL SOCIETY OF CHEMISTRY

www.rsc.org/advances

Graphical Abstract for

The Enhanced Photocatalytic Properties of BiOCl/$BiVO_4$ p-n Heterojunctions via Plasmon Resonance of Metal Bi

Chenchen Feng,[a,b] Dahui Wang, [*a] Bingjun Jin[a,b] and Zhengbo Jiao[*b]

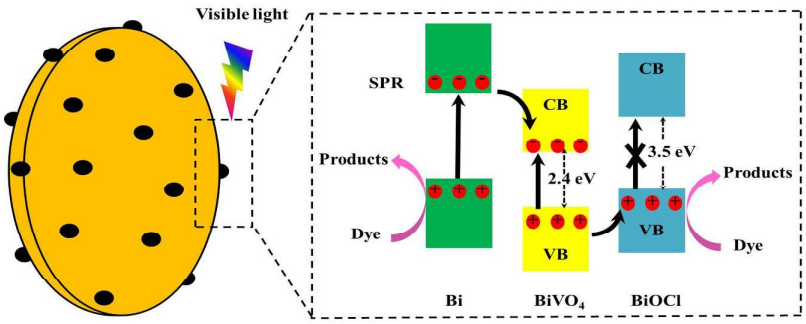

A novel p-n heterojunctions of BiOCl/$BiVO_4$ nanosheets have been firstly fabricated via one step method and the photocatalytic and photoelectrochemical activities can be further improved by depositing metallic Bi owing to its plasmon resonance and the improved charge separation.

Journal Name

RSCPublishing

ARTICLE

The Enhanced Photocatalytic Properties of BiOCl/$BiVO_4$ p-n Heterojunctions via Plasmon Resonance of Metal Bi

Cite this: DOI: 10.1039/x0xx00000x

Received 00th January 2012,
Accepted 00th January 2012

DOI: 10.1039/x0xx00000x

www.rsc.org/

Chenchen Feng,[a,b] Dahui Wang,[*a] Bingjun Jin[a,b] and Zhengbo Jiao[*b]

A novel p-n heterojunctions of BiOCl/$BiVO_4$ nanosheets have been firstly fabricated via one step method, which becomes a unified integration due to the substation process and exhibit higher photocatalytic performance than each pure component. Moreover, the photocatalytic and photoelectrochemical activities of BiOCl/$BiVO_4$ hybrids can be further improved by depositing metallic Bi owing to its plasmon resonance. Metallic Bi can not only furnish extra electrons to enhance the photocurrent but also supply an oxidation position to degrade organic contaminants. In addition, although BiOCl could not be excited by visible light, it could capture holes from the valance band of $BiVO_4$, which would effectively facilitate the separation of photogenerated electron-hole pairs and thus significantly improve the photocatalytic properties of $BiVO_4$.

Introduction

Over the past decades, there is considerable interest in the application of semiconductor photocatalysts for its virtue of their property of environmental cleaning and solar energy utilization.[1-3] It is well-know that $BiVO_4$ exists in three main crystalline phases, monoclinic scheelite, with a band gap energy of 2.4 eV, and the tetragonal zircon and tetragonal scheelite structures, both of which are currently under a band gap energy of 3.1 eV.[4,5] However, only monoclinic scheelite $BiVO_4$ (m-$BiVO_4$) was seen as an outstanding photocatalyst because of its applications in pigments, ionic conductivity, and ferro-elasticity.[6] Moreover, m-$BiVO_4$ is also an important semiconductor photocatalysts and has been of great interest for the photocatalytic water splitting and the photocatalytic degradation of organic pollutants under visible light illumination because of its narrow band gap ($E_g \approx 2.4$ eV) and feasible site of conduction band and valence band.[7-9] Beyond that, it is also nontoxic and chemically stable in aqueous solution under irradiation. Nonetheless, low separation efficiency of photogenerated electron-hole pairs, poor electrical conductivity and adsorptive performance, limiting wide application of pristine m-$BiVO_4$ in the fields of environmental protection and solar conversion.[10,11] More recently, numerous attempts have been made to enhance the photocatalytic activity of m-$BiVO_4$, including heterojunction structure formation,[12-19] loading co-catalysts,[20-21] and impurity doping.[23-28]

BiOCl is a layer-structured semiconductor with a tetragonal structure with lattice constants of a=b=3.883 Å and c=7.347 Å, consisting of tetragonal [Bi_2O_2] positively charged slabs which are interleaved by double slabs of chloride to form [Cl-Bi-O-Bi-Cl] layers along the c-axis，which forming a two dimensional nanoplate morphology, favoring the transfer of electrons and holes generated inside the crystal surface and promoting electron-hole separation.[29] It is unfortunate that BiOCl is a wide-band-gap ($E_g \approx 3.5$ eV) semiconductor and can only absorb ultraviolet light, which accounts for less than 5% of solar energies, leading to poor photocatalytic performance under visible light irradiation.[30,31] Good news is monoclinic scheelite $BiVO_4$ is normally an intrinsic n-type semiconductor, BiOCl is a p-type semiconductor, respectively.[32,33,34] Theo-retically, n-type $BiVO_4$ and p-type BiOCl can generate a p–n type heterojunction after being integrated with each other.[33]

Heterojunction structure, that is, contains two semiconducting oxides with variable band gap have proved to be a feasible approach.[18] Composite semiconductors produce dramatic changes in their electrical properties by increasing separation probability of photogenerated electrons and holes pairs. Thus heterojunction structure has been widely employed to improve the photocatalytic activity. For instance, BiOCl/$BiVO_4$, $CuCr_2O_4$/TiO_2, $BiVO_4$/Bi_2S_3, $BiVO_4$/Co_3O_4, $BiVO_4$/$CuCr_2O_4$ forming the p-n heterojunction structure have been demonstrated as effectual in separating electron and hole pairs.[12-14,18]

Lately, another approach to promote the separation of photogenerated charge carriers is adding metal nanoparticles, such as Ag, Au, and Pt, forming surface plutonic metallic nanostructures. From the related literature, the applications of excited plasmonic nanostructures in the field of photon-driven chemical conversion contains: (a) Plasmonic-metal-induced enhancements in the rates of photocatalytic water splitting on composite plasmonic-metal/semiconductor photocatalysts; and (b) direct, energetic electron-driven photocatalysis on plasmonic nanostructures.[29] Among reports of surface plasmonic metallic nanostructures, Ag/$BiVO_4$ hollow and porous composites were successfully synthesized via solvo-

thermal methods.[26] Besides, work devoted to bismuth metal deposited on BiOCl has been attempted.[30,31]

Herein, in the present work, we firstly developed the $BiOCl/BiVO_4$ nanosheets photocatalysts using a hydrothermal substitution method. Then, metallic Bi was in situ deposited on the $BiOCl/BiVO_4$ nanosheets by a poloalchohol reduction method and the ternary $Bi/BiOCl/BiVO_4$ nanosheets were obtained finally. More importantly, ternary nanosheets exhibits greatly enhanced activities in the visible-light driven photocatalytic degradation of RhB and photoelectrochemical characterization due to the plasmon resonance and the improved electron-hole pair separation.

Experimental Section

Materials

Bismuth nitrate pentahydrate ($Bi(NO_3)_3{\cdot}5H_2O$), bismuth trichloride($BiCl_3$), ammonium metavanadate(NH_4VO_3), ethanolamine($H_2NCH_2CH_2OH$), ammonium hydroxide (NH_4OH), ethylene glycol ($(CH_2OH)_2$), nitric acid (HNO_3), N,N-Dimethylformamide. All reagents used were analytically pure, and were purchased from Sinopharm Chemical Reagent Co. Ltd, and were utilized without further purification. Absolute ethanol and deionized water was used throughout this study.

Preparation of photocatalysts

The pure $BiVO_4$ was synthesized via a typical procedure, 1 mmol of $Bi(NO_3)_3{\cdot}_5H_2O$ and 1mmol of NH_4VO_3 was added to 30 mL of 2M nitric acid solution at room temperature and remained continuous stirring for 30 minutes. Then, an appropriate amount of NH_4OH (25～28%) was also added into the prepared solution to fit the pH value to 8. After stirring for 30 minutes to obtain a clear orange solution. This solution was poured into a 50 mL Teflon-lined autoclave and maintained at 180℃ for 24 h under autogenous pressure, and then naturally cooled to room temperature. The resulting precipitates were collected and washed with ethanol and deionized water thoroughly and dried at 80℃ in air. The as-obtained products were denoted m-$BiVO_4$.

The $BiOCl/BiVO_4$ nanosheets were synthesized by a similar method. In a typical procedure, 1mmol of $BiCl_3$ were added into 50 mL of deionized water under mild stir to form a white suspension due to the hydrolysis of $BiCl_3$. This solution was denoted solution A. At the same time, 1mmol of NH_4VO_3 was added into 30 mL of deionized water under continuous stir, this solution was denoted solution B. After two solutions were stirred for 10 minutes, solution B was added to solution A dropwise. Afterwards, the pH value of the mixture solution quickly reached 5.5, and the suspension changed into yellow when an appropriate amount of 1M aqueous ethanolamine was inserted. The mixture solution was maintained under mild stir for 30 minutes and then moved to 100 mL Teflon-lined autoclave. Finally underwent a hydrothermal treatment for 12 h at 160℃. The resulting precipitates were collected and washed with ethanol and deionized water thoroughly and dried at 80℃ in air. The as-obtained products were denoted $BiOCl/BiVO_4$.

Finally, the ternary $Bi/BiOCl/BiVO_4$ ternary nanosheets were synthesized via a typical reflux synthesis process, 0.5 g of $BiOCl/BiVO_4$ was added into 100 mL of ethylene glycol and underwent a reflux treatment for X h at 200℃. The resulting precipitates were collected and washed with ethanol and deionized water thoroughly and dried at 80℃ in air. The as-obtained products were denoted X-$Bi/BiOCl/BiVO_4$.

Characterization

The X-ray diffraction spectra (XRD) measurements were made on a Rigaku RINT-2000 instrument utilizing Cu Kα radiation (40 KV). The XRD patterns were recorded from 10° to 90° with a scanning rate of 0.067°/s. Scanning electron microscopy (SEM) measurements were carried out on a field-emission scanning electron microscope (JSM-6701F.JEOL) used at an accelerating voltage of 5 KV. Transmission electron microscopy (TEM) measurements were performed by using a FEI Tecnai TF20 microscope operated at 200 kV. UV-vis diffuse reflectance spectra were made on an UV-2550 (Shimadzu) spectrometer by using $BaSO_4$ as the reference. The element composition was observed by X-ray photoelectron spectroscope (XPS. Kratos Axis Ultra DLD).

Photocatalytic activity measurements

In all photocatalytic degradation of RhB, 0.2 g of the samples were added into a solution of RhB dyes (100 mL, 8mg/L), Prior to irradiation, the solution was stirred in the dark for 0.5 h to ensure the adsorption-desorption equilibrium had been reached. Then，this solution was irradiated with a 300 W Xe arc lamps equipped with an ultraviolet cutoff filter to provide visible light with $\lambda \geqslant 420$ nm. During the degradation of organic dyes, the solution with the samples was continuously stirred with a magnetic stirrer and the concentration of RhB was monitored by UV/Vis spectroscopy (UV-2550PC. Shimadzu). The photocatalysts were removed from the photocatalytic reaction systems by a dialyzer before the spectroscopy measurement.

Photoelectrochemical measurements

The photoelectrical was prepared by drop-casting method on FTO substrate (1.5×2.5 cm^2), as the working electrode, were cleaned by ultrasonication in distilled water, acetone and ethanol for 20 min sequentially. 20 mg of photocatalyst powders were dispersed in 0.2 mL of N, N-Dimethylformamide under sonication for 1 h to produce a slurry. The as-prepared slurry was dispersed onto the conductive surface of the FTO glass to form a photocatalyst film. Subsequently, the photoelectrodes were dried in an oven at 200℃ for 60 min.

The photocurrents were calculated by an electrochemical analyzer (CHI660D) in a standard three-electrode system with a working electrode, a Pt foil as the counter electrode, and a saturated calomel electrode (SCE) as a reference electrode. A 300 W Xe arc lamps (HSX-F/UV 300) was utilized as a light source. Illumination through the FTO side (back-side illumination) was utilized. A 0.25 M Na_2SO_4 and 0.25 M Na_2SO_3 mixture solution was invoked as the electrolyte.

Results and discussion

The X-ray diffraction (XRD) pattern of the products displayed in Figure 1 and Fig. S1. All of the sharp diffraction peaks in the XRD pattern are perfectly in good agreement with standard data of monoclinic $BiVO_4$ (JCPDS, No. 83-1699), BiOCl (JCPDS, No. 73-2060) and Bi (JCPDS, No. 85-1329). No peaks of additional phases were identified in the as-synthesized samples. Moreover, according to the intensity of peaks in Fig. 1, the m-$BiVO_4$ phase is the main phase in the 1-

Bi/BiOCl/$BiVO_4$. Moreover, compared with the relative strength showed in the standard patterns, it can be seen that the peaks indexed as (001), (002), (003) of BiOCl and (004) of $BiVO_4$ show the obvious enhancement of intensity. It is inferred that the BiOCl/ $BiVO_4$ prefers orientated growth along the {001} facet, which is vertical to the nanosheets. Therefore, we can say that the as-synthesized products have a preferred orientation along the (001) planes, it is the evidence that the morphologies of the ternary Bi/BiOCl/$BiVO_4$ composite is nanosheets. In some previous reports, for BiOCl or $BiVO_4$ nanosheets, the superior hydrophilic ability or higher surface energy of (001) planes might result in high photocatalytic activity.[30,32] In addition, we can see that the contents of Bi continuously increase when prolonging reaction time (Fig. S1b).

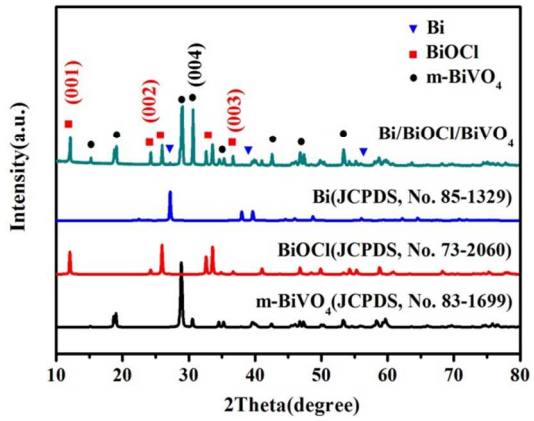

Fig. 1 XRD patterns of the as-synthesized Bi/ BiOCl/$BiVO_4$, standard XRD pattern of Bi (JCPDS, No. 85-1329), BiOCl (JCPDS, No. 73-2060), and m-$BiVO_4$ (JCPDS, No. 83-1699).

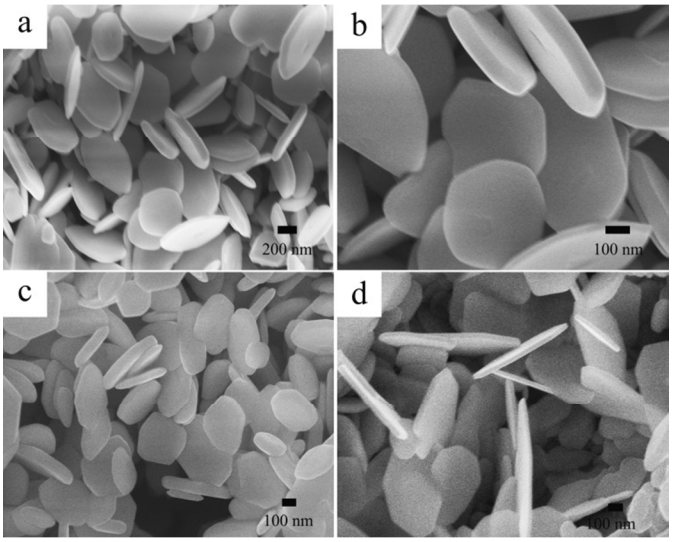

Fig. 2 Low and high-magnification SEM images of (a, b) BiOCl/$BiVO_4$ and (c, d) Bi/BiOCl/$BiVO_4$.

The morphologies of all samples were examined by SEM. It can be seen in Fig. 2 that the as-synthesized BiOCl/$BiVO_4$ and Bi/BiOCl/$BiVO_4$ are composed of nanosheets with 500-1000 nm in width and 10-100 nm in thickness. Likewises, Fig. S2 shows the morphologies of pure $BiVO_4$, 0.5, 2 and 3-Bi/BiOCl/$BiVO_4$. The SEM results suggest that the morphology or particle size of the ternary Bi/BiOCl/$BiVO_4$ composites shows slight changes.

Transmission electron microscopy (TEM) images (Fig. 3a, 3b) analysis further showed the nanosheets structure of the as-synthesized ternary Bi/BiOCl/$BiVO_4$ composite. In order to reveal the spatial distribution of the Bi, BiOCl and $BiVO_4$ phases in the nanosheets structure, the EDS elemental mapping was performed on a ternary Bi/BiOCl/$BiVO_4$ nanosheets. It can be seen from Fig. 3c-3f, the mapping results shows uniform distribution of Bi, V, O, Cl elements throughout the ternary Bi/BiOCl/$BiVO_4$ nanosheets. Otherwise, EDX elemental line mapping of the Bi/BiOCl/$BiVO_4$ nanosheets was showed in the Fig. S3, it can also confirm the homogeneous distribution of the four elements. These results demonstrate that BiOCl and $BiVO_4$ are uniformly distributed in the whole nanosheets and the metal Bi nanoparticles deposited on the external surface of the nanosheets.

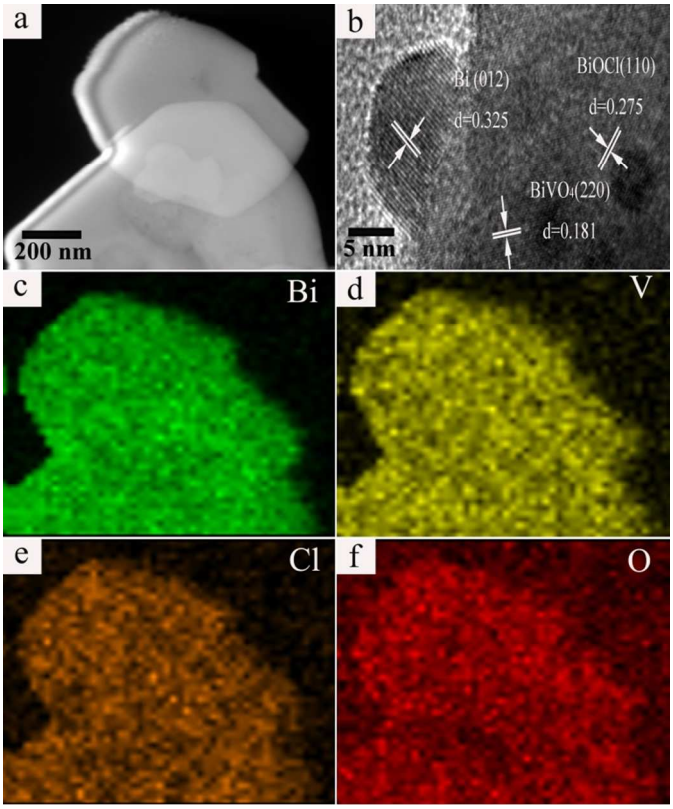

Fig. 3 (a, b) TEM images of the as-obtained Bi/BiOCl/$BiVO_4$ and the corresponding elemental mapping images of (c) Bi, (d) V, (e) Cl, and (f) O elements.

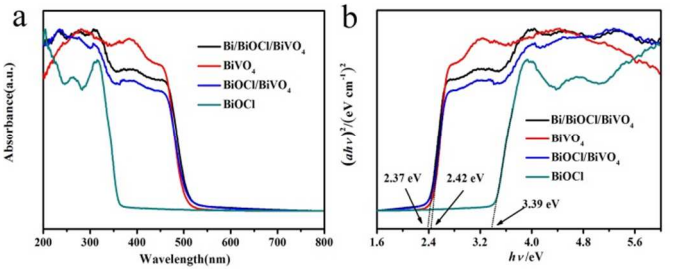

Fig. 4 (a) UV-vis diffuse reflectance spectra (DRS) of Bi/BiOCl/$BiVO_4$, BiOCl/$BiVO_4$, m-$BiVO_4$ and BiOCl. (b) Plot

of the transformed Kubelka–Munk functions vs. the energy of light.

Additionally, the photocatalytic performance of samples was strongly connected with the optical absorption property.[33] Therefore, UV-vis diffuse reflectance spectra (DRS) was utilized to further investigate the absorption band the band gap energy (E_g) values of the crystals. It can be seen from Fig. 4a that all of the four samples showed absorption bands in the visible light region, and the absorption edges of the samples exhibit a slight red shift when the presence of Bi. The optical band gap energies of the four samples were estimated from the absorption spectra by using the following relationship: $ahv=A(hv-E_g)^{n/2}$ where α, hv, A, and E_g are the absorption coefficient, the photon energy, constant, and the optical band gap energy, respectively. The value of n depends on whether the transition is direct (n=1) or indirect (n=4), and it was determined to be unity on the absorption spectra. The band gap energy was determined by extrapolating the linear part of $(ahv)^2$ vs. hv plot of the energy axis at a=0 as showed in Fig. 4b. According to the Tauc plot, the estimated E_g values of the samples were similar, around 2.37 to 2.42 eV, corresponding to Bi/BiOCl/$BiVO_4$ composite and pure m-$BiVO_4$, respectively. The 2.42 eV value for pure m-$BiVO_4$ is in agreement with the literature.[34] Thereby, it can be known that the ternary Bi/BiOCl/$BiVO_4$ nanocomposites possess narrower band gap than pure $BiVO_4$ nanoparticls.

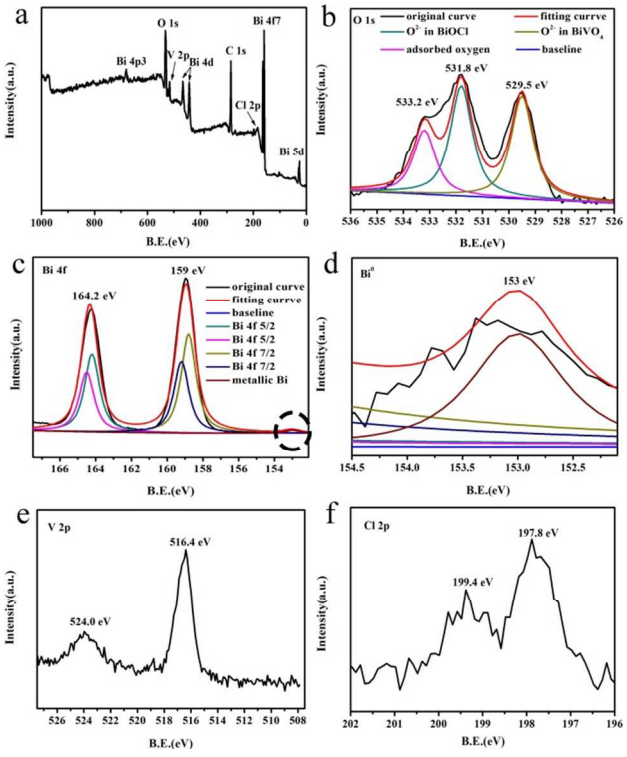

Fig. 5 XPS spectra of the as-prepared 1-Bi/BiOCl/$BiVO_4$ composite: (a) typical XPS survey, (b) O 1s spectra, (c) Bi 4f spectra, (d) partial enlarged detail of (c), (e) V 2p and (f) Cl 2p spectra.

Owing to the elementary composition of the Bi/BiOCl/$BiVO_4$ composite was investigated by XPS spectrum, the results of which were shown in Fig. 5. It can be seen that only C, Bi, O, V and Cl were detected in the composite from the XPS survey (Fig. 5a), and the C 1s peak at around 284.6 eV can be attributed to the signal that was used for calibration. XPS signals for O 1s at binding energy of 529.5 eV, 531.8 eV, 533.2 eV, corresponding to $\cdot O^{2-}$ in $BiVO_4$, BiOCl and adsorbed oxygen in the surface of the composites. Two strong peaks in the Fig. 5c, at 164.28 eV and 159 eV, are indexed to Bi 4f5/2 and Bi 4f7/2, besides, a weak peak (Fig. 5d) at 153 eV, are indexed to Bi^0, which demonstrates that the bismuth species in the 1-Bi/BiOCl/$BiVO_4$ composite is Bi^{3+} cations and metallic Bi particles. The characteristic Spin−Orbit splitting of V 2p1/2 and V 2p3/2 signals is observed at approximately 524.0 and 516.4 eV, respectively, corresponding to V^{5+} in $BiVO_4$ (Fig. 5e). In addition, binding energy of 199.4 eV and 197.8 eV are indexed to Cl 2p1/2 and Cl 2p3/2, which suggests that chlorin species in the BiOCl are Cl^- anions (Fig. 5f). Apparently, the XPS results are in agreement with those of the XRD results and TEM results, further demonstrating the co-existence of Bi, BiOCl and $BiVO_4$ in the composite.

The photocatalytic activity of the samples was evaluated by the photodegradation of rhodamine B (RhB) dye in aqueous solution (8 mg/L) (Fig. 6) under visible light ($\lambda > 420$ nm) irradiation. For comparison, photocatalytic performances of m-$BiVO_4$, BiOCl and BiOCl/$BiVO_4$ nanosheets have also been investigated. As showed in Fig. 6a, it can be clearly seen that the ternary Bi/BiOCl/$BiVO_4$ nanosheets show better photocatalytic performance than the other samples. RhB was almost completely degraded after 40 min of visible light irradiation. Such superior photocatalytic activities could be attributed to the good crystallization with fewer structural defects and preferred crystal facets for surface-controlled photocatalysis. These results clearly demonstrate that the photocatalytic activity of BiOCl/$BiVO_4$ nanosheets can be further enhanced by depositing Bi on the BiOCl/$BiVO_4$ nanosheets surface in situ. In addition, comparison of photocatalytic performances for the ternary BiOCl/$BiVO_4$ nanosheets with different reaction time (Fig. S4).

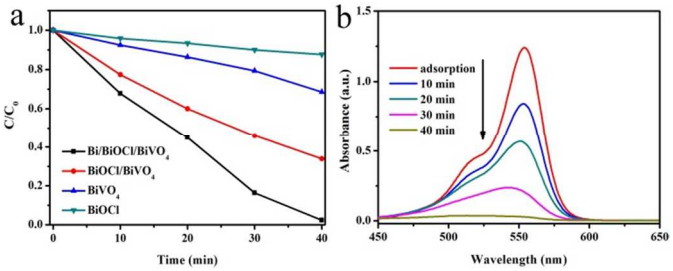

Fig. 6 (a) The photocatalytic degradation of RhB over various photocatalysts under visible-light illumination, (b) temporal UV-visible absorption spectral changes of RhB dye over Bi/BiOCl/$BiVO_4$ at different irradiation time.

Furthermore, the photocurrent transient response measurement of m-$BiVO_4$, BiOCl and BiOCl/$BiVO_4$ nanosheets and the ternary Bi/BiOCl/$BiVO_4$ nanosheets was performed. Fig. 7 shows the rapid and consistent photocurrent responses for each light-on and off event in multiple 20 s on-off cycles under visible light illumination. It is worth to note that the photocurrent density of the ternary Bi/BiOCl/$BiVO_4$ nanosheets electrode (ca. 130 $\mu A/cm^2$) is about thrice and twice that of the m-$BiVO_4$ (ca. 43 $\mu A/cm^2$) and BiOCl/$BiVO_4$ nanosheets (ca. 63 $\mu A/cm^2$) electrodes, respectively. It is well known that the photocurrent response is produced mainly by the diffusion of the photogenerated electrons to the FTO, and meanwhile the photogenerated holes are captured by the hole acceptor in the

electrolyte.[32] So the enhanced photocurrent response of the as-prepared ternary Bi/BiOCl/$BiVO_4$ nanosheets demonstrates higher separation efficiency of the photogenerated electron–hole pairs and a lower recombination rate in such hybrid structures under visible-light illumination.[35] Meanwhile, the order of the photocurrent strengths is in keeping with the photocatalytic performances. In addition, the comparison of the photocurrent transient response for the ternary BiOCl/$BiVO_4$ nanosheets with different reaction time (Fig. S5).

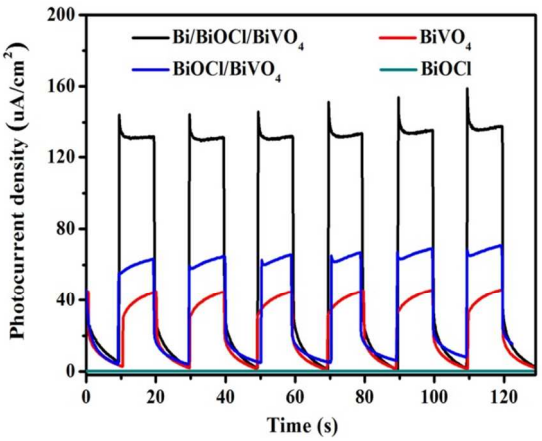

Fig. 7 Photocurrent response of the Bi/BiOCl/$BiVO_4$, m-$BiVO_4$, BiOCl/$BiVO_4$ and BiOCl in a 0.25 M Na_2SO_4 and 0.25 M Na_2SO_3 mixture solution at a bias of 0.8V vs. SCE under visible light illumination.

A possible photocatalytic mechanism has been proposed in schematic given below (Fig. 8). On the one hand, m-$BiVO_4$ is normally an intrinsic n-type semiconductor, and BiOCl is a p-type semiconductor. When n-type $BiVO_4$ and p-type BiOCl generate a p-n type heterojunction after integrated with each other. At the same time, an internal static electric field ($E_{internal}$) is formed at the interface between them, with electric field direction from $BiVO_4$ to BiOCl. Due to the Fermi level of $BiVO_4$ close to its' conduction band, but the Fermi level of BiOCl close to its' valence band, so the Fermi level of $BiVO_4$ is higher than that of BiOCl. When the heterostructure is generated, electrons will transfer from the side with the higher Fermi level to the side with the lower Fermi level and holes will flow from the side with the lower Fermi level to the side with the higher Fermi level. This leads to the Fermi levels on both sides become the same.[14] This type of p-n heterojunction has been used to reduce the recombination probability of photogenerated electrons and holes. However, the separation of photogenerated charge carriers strongly depends on the band-edge positions of the two semiconductors.

Depending on the previous reports, the positions of the valence band and the conduction band of $BiVO_4$ and BiOCl are approximately 2.75, 0.33 eV and 2.4, -1.1 eV, respectively.[5,36] In addition, it has been reported that the BiOCl is a potential photocatalyst in decomposing organics under UV light irradiation.[37] Thus it is seen in the $BiVO_4$/BiOCl that BiOCl work as a main photocatalyst, while the role of $BiVO_4$ is a sensitizer absorbing visible light. Under visible-light irradiation ($\lambda > 420$ nm), the photogenerated electrons would be excited from the VB to CB of $BiVO_4$ and the VB of $BiVO_4$ becomes partially vacant, and the holes from the VB of $BiVO_4$ can be transferred to VB of BiOCl. As a result, holes are generated in the VB of BiOCl, and initiate photocatalytic oxidation reactions. Interestingly, due to the plasma effect of metal Bi on BiOCl/$BiVO_4$ nanosheets surface, the photogenerated electrons would transfer to CB of $BiVO_4$ from metal Bi. We can see from Fig. 8 that the existence of Bi not only provides extra active sites for oxidation reaction, but also promotes the transfer of photogenerated electrons for photocurrent responds. On the basis of above analysis, the photogenerated electrons and holes could be effectively separated in this hybrid structure.

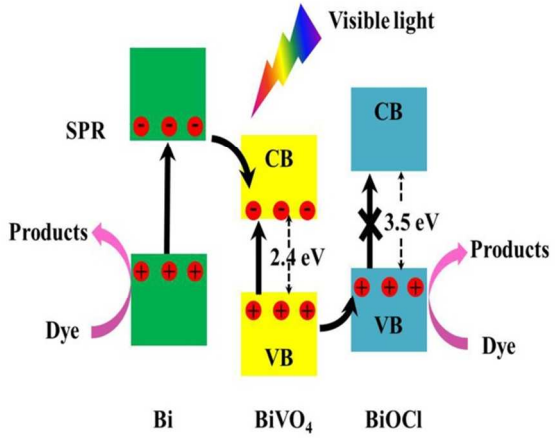

Fig. 8 A proposed schematic mechanism for photocatalytic reactions happened on Bi/BiOCl/$BiVO_4$.

Conclusions

In summary, we have investigated novel ternary Bi/BiOCl/$BiVO_4$ hybrid nanosheets including a p-n heterojunction and a plasmonic metal. Compared with pure photocatalyst, the as-obtained Bi/BiOCl/$BiVO_4$ nanosheets showed the best photocatalytic activity for reduction of RhB and photocurrent response under visible-light illumination. All of the results indicate that the enhancement of the photocatalytic activity and photocurrent response is attributed to the formation of hybrid structures, leading to an effective separation of photogenerated electrons and holes. These findings may open up a new avenue for the morphology control and structural design of $BiVO_4$ photocatalyst.

Acknowledgements

This work was supported by the "Hundred Talents Program" of the Chinese Academy of Science and the National Natural Science Foundation of China (21273255, 21303232).

Notes and references

[a]*School of Materials Science and Engineering, Lanzhou University of Technology, Lanzhou 730050, China.*
[b]*State Key Laboratory for Oxo Synthesis & Selective Oxidation, National Engineering Research Center for Fine Petrochemical Intermediates, Lanzhou Institute of Chemical Physics, CAS, Lanzhou 730000, China.*
E-mail: jiaozhb@licp.cas.cn

† Electronic Supplementary Information (ESI) available: additional figures. See DOI: 10.1039/b000000x/

1 F. E. Osterloh, *Chem. Soc. Rev*, 2013, **42**, 2294-2320.

2 A. Fujishima, X. T. Zhang and A. D. Tryk, *Int. J. Hydrogen Energy*, 2007, **32**, 2664-2672.
3 G. R. Xu, J. N. Wang and C. J. Li, *RSC Adv*, 2013, **3**, 12985-12992.
4 Martínez-de la Cruz, A. García-Pe·rez, U. M. Sepu·lveda-Guzma·n, S. Res. *Chem. Intermed*, 2012, **39**, 881−894.
5 S. Tokunaga, H. Kato and A. Kudo, *Chem. Mater*, 2001, **13**, 4624−4628.
6 Y. T. Yeom, S. H. Choh, M. L. Du and M. S. Jang, *Phys. Rev. B: Condens. Matter*, 1996, **53**, 3415.
7 K. Hirota, G. Komatsu, M. Yamashita, H. Takemura and O. Yamaguchi, *Mater. Res. Bull*, 1992, **27**, 823.
8 K. Sayama, A. Nomura, Z. G. Zou, R. Abe, Y. Abe and H. Arakawa, *Chem. Commun*, 2003, 2908.
9 A. Kudo, K. Omori and H. Kato, *J. Am. Chem. Soc*, 1999, **121**, 11459.
10 Y, Park. K. J. McDonald and K-S. Choi, *Chem. Soc. Rev*, 2013, **42**, 2321-2337.
11 M. C. Long, W. M. Cai, J. Cai, B. X. Zhou, X. Y. Chai, Y.H. Wu, *J. Phys. Chem. B*, 2006, **110**, 20211-20216.
12 X. Gao, H. B. Wu, L. Zheng, Y. Zhong, Y. Hu, X. Wen (David) Lou. *Angew. Chem. Int. Ed*, 2014, **53**, 5917-5921.
13 Z. He, Y. Shi, C. Gao, L. Wen, J. Chen, S. Song. *J. Phys. Chem. C*, 2014, **118**, 389-398.
14 R. Bajaj, M. Sharma, D. Bahadur. *Dalton Trans*, 2013, **42**, 6736-6744.
15 J. Wang, F. E. Osterloh. *J. Mater. Chem. A*, 2014, **2**, 9405.
16 S. J. Hong, S. Lee, J. S. Jang, J. S. Lee, *Energy Environ. Sci*, 2011, **4**, 1781-1787.
17 M. Long, W. Cai, H. Kisch, *J. Phys. Chem. C*, 2008, **112**, 548-554.
18 J. Yan, L. Zhang, H. Yang, Y. Tang, Z. Lu, S. Guo, Y. Dai, Y. Han and M. Yao, *Sol. Energy*, 2009, **83**, 1534-1539.
19 H. Q. Jiang, H. Endo, H. Natori, M. Nagai, K. Kobayashi, *Mater. Res. Bull*, 2009, 44, 700-706.
20 H. Xu, H. Li, C. Wu, J. Chu, Y. Yan, H. Shu, Z. Gu, *J. Hazard. Mater*, 2008, **153**, 877-884.
21 S. Kohtani, M. Tomohiro, K. Tokumura, R, Nakagaki, *Appl. Catal. B*, 2005, **58**, 265-272.
22 S. Kohtani, J. Hiro, N. Yamamoto, A. Kudo, K. Tokumura, R. Nakagaki, *Catal. Commun*, 2005, **6**, 185-189.
23 W. Yao, H. Iwai, J. Ye, *Dalton Trans*, 2008, 1426-1430.
24 W. Yao, J. Ye, *J. Phys. Chem. B*, 2006, **110**, 11188-11195.
25 W. Luo, Z. Yang, Z. Li, J. Zhang, J. Liu, Z. Zhao, Z. Wang, S. Yan, T. Yu, Z. Zou, *Energy Environ. Sci*, 2011, **4**, 4046-4051.
26 L. Chen, R. Huang, Y. Ma, S. Luo, C. Auab, S. Yin. *RSC Adv*, 2013, **3**, 24354.
27 D. Tang, H. Zhang, H. Huang, R. Liu, Y. Han, Y. Liu, C. Tong, Z.Kang. *Dalton Trans*, 2013, **42**, 6285.
28 S. Huang, N. Zhu, Z. Lou, L. Gu, C. Miao, H. Yuan, A. Shan. *Nanoscale*, 2014, **6**, 1362.
29 F. Dong, Y. J. Sun, M. Fu, Z. B. Wu, S. C. Lee, *J. Hazard. Mater*, 2012, **219−220**, 26−34.
30 J. Jiang, K. Zhao, X. Y. Xiao, L. Z. Zhang, *J. Am. Chem. Soc*, 2012, **134**, 4473−4476.
31 S. Shenawi-Khalil, V. Uvarov, E. Menes, I. Popov, Y. Sasson, *Appl. Catal. A*, 2012, **413−414**, 1−9.
32 G. C. Xi and J. H. Ye, *Chem. Commun*, 2010, **46**, 1893–1895 | 1893.
33 Chen, L.; Zhang, Q.; Huang, R.; Yin, S.-F.; Luo, S.-L.; Au, C.-T. *Dalton Trans*.2012, 41, 9513.
34 C. R. Michel, N. L. L. Contreras, A. H. Martínez-Preciado, *Sens. Actuators B*, 2011, **160**, 271−277.
35 M.-L. Guan, D.-K. Ma, S.-W. Hu, Y.-J. Chen, S.-M. Huang, *Inorg. Chem*, 2011, **50**, 800−805.
36 S. Linic, P. Christopher, D. B. Ingram. *Nature materials*, 2011, **10(12)**: 911-921.
37 S. Weng, B. Chen, L. Xie, Z. Zheng, P. Liu. *J. Mater. Chem. A*, 2013, **1**, 3068.

